Open Research Online

Astronomically paced changes in overturning circulation in the Western North Atlantic during the middle Eocene

Journal Item

For guidance on citations see FAQs.

Version: Version of Record

oro.open.ac.uk

Astronomically paced changes in deep-water circulation in the western North Atlantic during the middle Eocene

Maximilian Vahlenkamp [a,*], Igor Niezgodzki [b,c], David De Vleeschouwer [a], Torsten Bickert [a], Dustin Harper [d], Sandra Kirtland Turner [e], Gerrit Lohmann [b], Philip Sexton [f], James Zachos [d], Heiko Pälike [a]

[a] *MARUM - Center for Marine Environmental Sciences, University of Bremen, Leobener Str. 8, 28359 Bremen, Germany*
[b] *Alfred Wegener Institute - Helmholtz Centre for Polar and Marine Research, Bussestr. 24, 27570 Bremerhaven, Germany*
[c] *ING PAN - Institute of Geological Sciences, Polish Academy of Sciences, Research Center in Kraków, Biogeosystem Modelling Laboratory, Kraków, Poland*
[d] *Department of Earth & Planetary Science, University of California, Santa Cruz, CA 95064, USA*
[e] *Department of Earth Sciences, University of California, Riverside, CA 92521, USA*
[f] *School of Environment, Earth & Ecosystem Sciences, The Open University, Milton Keynes MK7 6AA, UK*

A B S T R A C T

North Atlantic Deep Water (NADW) currently redistributes heat and salt between Earth's ocean basins, and plays a vital role in the ocean-atmosphere CO_2 exchange. Despite its crucial role in today's climate system, vigorous debate remains as to when deep-water formation in the North Atlantic started. Here, we present datasets from carbonate-rich middle Eocene sediments from the Newfoundland Ridge, revealing a unique archive of paleoceanographic change from the progressively cooling climate of the middle Eocene. Well-defined lithologic alternations between calcareous ooze and clay-rich intervals occur at the $\sim$41-kyr beat of axial obliquity. Hence, we identify obliquity as the driver of middle Eocene (43.5–46 Ma) Northern Component Water (NCW, the predecessor of modern NADW) variability. High-resolution benthic foraminiferal $\delta^{18}O$ and $\delta^{13}C$ suggest that obliquity minima correspond to cold, nutrient-depleted, western North Atlantic deep waters. We thus link stronger NCW formation with obliquity minima. In contrast, during obliquity maxima, Deep Western Boundary Currents were weaker and warmer, while abyssal nutrients were more abundant. These aspects reflect a more sluggish NCW formation. This obliquity-paced paleoceanographic regime is in excellent agreement with results from an Earth system model, in which obliquity minima configurations enhance NCW formation.

1. Introduction

Modern North Atlantic Deep Water (NADW) production accounts for $\sim$40 to 50% of Atlantic Meridional Overturning Circulation (AMOC) (Broecker, 1998). As an important part of global thermohaline circulation, the AMOC helps regulate global climate in three primary ways: i) through the zonal and latitudinal redistribution of heat, salt, and nutrients (Broecker and Peng, 1982), ii) via the carbon cycle, by AMOC's dominant role in moderating oceanic CO_2 uptake (Zickfeld et al., 2008) and iii) by its effect on atmospheric circulation through modulation of global sea surface temperatures (SST) (Mulitza et al., 2008). Accordingly, variations in AMOC intensity can cause large-scale perturbations to global and regional climates.

Ocean circulation has evolved in response to changes in paleogeographic configurations over time. During the early Paleocene, the oceanic connection between the Greenland-Norwegian Sea and the North Atlantic was not yet established and the Atlantic was a much narrower elongated basin with extended adjacent shallow shelf areas (Scotese et al., 1988). Overturning principally occurred in the Southern Ocean during the late Paleocene to early Eocene (Pak and Miller, 1992; Thomas et al., 2003), with possible contribution of deep-water sources in the North Pacific (Thomas, 2004) and warm saline deep water originating in the Tethys (Scher and Martin, 2004). Extremely high deep ocean temperatures (up to 12 °C higher than modern) (Cramer et al., 2011; Sexton et al., 2006a; Zachos et al., 2001) and elevated atmospheric CO_2 (Anagnostou et al., 2016) were associated with decreased latitudinal temperature gradients (Tripati and Elderfield, 2005) and an enhanced hydrological cycle (Barron et al., 1989) that freshened the surface ocean at high latitudes. During the early Eocene, rifting in the Greenland-Norwegian Sea (Mosar et al., 2002) created the

necessary paleogeographic preconditions for the onset of a deep-water source in the North Atlantic. In addition, global cooling increased the importance of sea surface salinity relative to sea surface temperature in the formation of deep water (De Boer et al., 2007), thus accentuating the potential for deep-water formation in the North Atlantic (De Boer et al., 2008). The input of mechanical energy triggered by winds, tides and eddies induces diapycnal mixing (Kuhlbrodt et al., 2007), adding to the buoyancy forcing, which results from differences in water temperature and salinity. This mixing drives the exchange between the surface ocean and deeper layers through overturning and upwelling of deep-water masses around the Antarctic Circumpolar Current (Toggweiler and Bjornsson, 2000; Toggweiler and Samuels, 1998). The modern four layer ocean structure and increased export of Northern Component Water to the South Atlantic has been related to the development of the Antarctic Circumpolar Current during the late Eocene to early Oligocene when the Drake and Tasman Passages began to open (Cramer et al., 2009; Katz et al., 2011; Scher and Martin, 2008). Davies et al. (2001) proposed an onset of NCW at 35 Ma based on the identification and dating of the at this time oldest known North Atlantic Drift Sediments. Nd isotopes from the South Atlantic and the Southern Ocean have later been used to verify this age (Via and Thomas, 2006). However, the South Atlantic was less radiogenic (as characteristic of NCW) during the middle Eocene than during the Oligocene (Scher and Martin, 2008; Via and Thomas, 2006). Hohbein et al. (2012) pushed back the date of the onset of NCW based on the onset of sediment drift deposits within a restricted sedimentary basin at the Greenland–Scotland Ridge, a key gateway for modern NADW outflow into the North Atlantic. This age close to the early-middle Eocene boundary is supported by the onset of the Newfoundland Drifts (Boyle et al., 2017) and winnowing at Blake Nose as indicated by the deposition of foraminiferal sands which have been deposited across the early–middle Eocene boundary disconformity (Norris et al., 2001). The proposed timing of first NCW at the early-middle Eocene boundary coincides with the invigoration of bottom currents inferred by large scale erosion in the North Atlantic (Berggren and Hollister, 1974), the onset of the Cenozoic global deep-water cooling trend (Zachos et al., 2001), major changes in deep-sea circulation as evident through changes in the global inter-basinal δ^{13}C gradient (Sexton et al., 2006a) warming of the Atlantic relative to Pacific bottom waters (Cramer et al., 2009) and enhanced global productivity (Nielsen et al., 2009).

Most attempts to characterize the oceanic response to astronomical forcing under greenhouse conditions during the Cenozoic have focused on the early Eocene greenhouse, before the onset of NCW formation (e.g. Lunt et al., 2011; Sloan and Huber, 2001). Here, we particularly focus on the response to changes in obliquity (i.e. the tilt of Earth's rotational axis) after the onset of NCW (Boyle et al., 2017; Hohbein et al., 2012).

The effect of obliquity is largest at high latitudes, where the climate response to obliquity forcing is enhanced by various feedback mechanisms (Mantsis et al., 2011). Several mechanisms including atmospheric and ocean circulation are known to transfer high latitude insolation forcing into mid or low latitudinal climate signals (Liu and Herbert, 2004). During the Pleistocene, overturning in the North Atlantic was hampered by freshwater release from ice sheet collapse during intervals with unusually warm summers caused by maxima in obliquity (Sigman et al., 2007). Furthermore, in pre-Pleistocene times when Northern Hemisphere ice sheets were absent or smaller, cooler global temperatures are usually associated with minima in obliquity (De Vleeschouwer et al., 2017; Hays et al., 1976) facilitating sea ice formation and thus stimulating NCW formation. This is consistent with strong NADW formation during early Pliocene (4.7–4.2 Ma) obliquity minima (Billups et al., 1997). In the absence of continental ice sheets, obliquity can regulate the
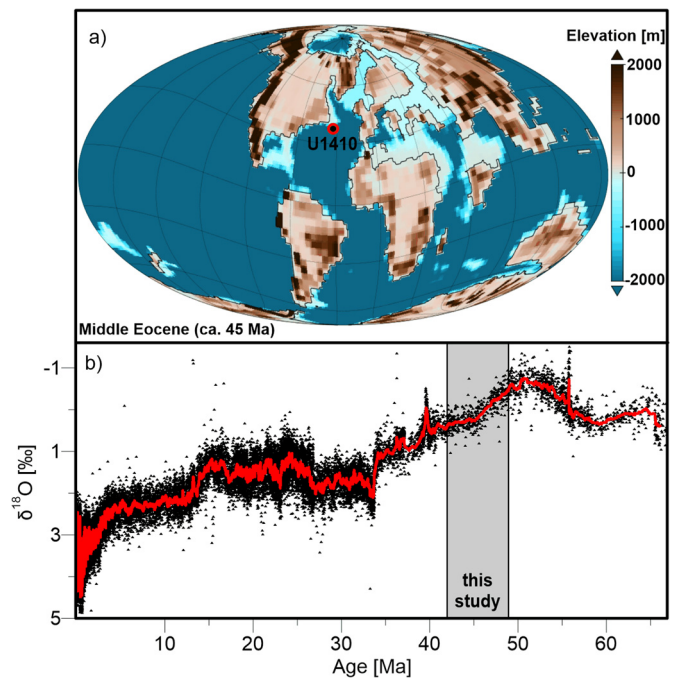

Fig. 1. Paleoclimate setting of the middle Eocene (45 Ma). a) Global topography and bathymetry used for middle Eocene model simulations in this study (modified after Lunt et al., 2016). b) The middle Eocene is characterized by the long-term cooling after the warmest climates of the Cenozoic, as indicated by a global compilation of Cenozoic $\delta^{18}O_{benthic}$ records (Cramer et al., 2009).

strength of the thermohaline circulation via its influence on temperature and density gradients, the hydrological cycle, the extent of sea ice, and possibly via the carbon cycle (Kuhlbrodt et al., 2009; Rahmstorf, 1995).

Sediments at Site U1410, drilled during IODP Expedition 342 at the Newfoundland Ridge (Norris et al., 2014) provide a unique opportunity to study middle Eocene deep ocean circulation in the western North Atlantic on orbital timescales. Here, we use the X-ray fluorescence (XRF) derived ratio of Ca/Fe in bulk sediment and benthic foraminiferal stable carbon and oxygen isotopes to constrain the intensity of the Deep Western Boundary Currents as well as deep-water nutrient availability and paleotemperature. Together, these allow us to infer orbital-scale variations in deep ocean circulation in the western North Atlantic during an interval of middle Eocene cooling. We establish the deep-water response to astronomical parameters and complement our observations with simulations using the coupled Earth system model *COSMOS*.

2. Material and methods

Site U1410 (41°19.6993′N, 49°10.1847′W; ~3387.5 m water depth) (Fig. 1) was drilled during Integrated Ocean Drilling Program (IODP) Expedition 342 – Paleogene Newfoundland Sediment Drifts (Norris et al., 2014). Middle Eocene sedimentation at this site occurred at a paleodepth of ~2950 m at ~50 Ma (Norris et al., 2012; Tucholke and Vogt, 1979). The recovered middle Eocene sediments hold a record of carbonate-rich, cyclic sequences. Moreover, relatively high sedimentation rates (2–4 cm/kyr) (Norris et al., 2014) characterize these sediments, allowing for a high-resolution reconstruction of oceanographic and climatic change.

2.1. XRF data

X-ray fluorescence measurements in the studied intervals were carried out on the Avaatech XRF Core Scanner at Scripps Institution of Oceanography Geological Collections, U.C. San Diego. Elemental

intensities were collected every 2 cm (ca. 1 kyr/sample) down-core over a 1.2 cm^2 area with a down-core slit size of 10 mm using generator settings of 10 kV and a current of 0.1 mA. The split surface of the archive half was covered with a 4 µm thick SPEXCerti Prep Ultralene 1 foil to avoid contamination of the XRF measurement unit and desiccation of the sediment. The sampling time at the split core surface was 20 seconds.

2.2. Isotope sampling strategy and chronology

For benthic foraminifer stable isotopes, we sampled the sedimentary record of Site U1410 at 4 cm intervals (ca. 2 kyr/sample). Some samples were taken from sections that are not incorporated in the latest version of the splice, as the initial shipboard splice was revised based on onshore-acquired XRF data (Supplementary Tables 1 and 2). We aligned all cores of Site U1410 on a centimeter scale to the depth scale of this revised splice (Supplementary Fig. 1 and Supplementary Table 3). All isotope data are placed on a common depth scale, and are directly comparable to other geochemical measurements presented here, though not consistently obtained from the same hole.

We updated the shipboard age model for Site U1410 by using the GTS 2012 Astronomic Age Model (Gradstein et al., 2012) ages of chron boundaries: 42.351 Ma for C19r/20n (131.76 mcd in Hole U1410A); 43.505 Ma for C20n/C20r (163.86 mcd in Hole U1410A); 45.942 Ma for C20r/C21n (218.40 mcd in Hole U1410A); 47.837 Ma for C21n/C21r (252.53 mcd in Hole U1410A) (Norris et al., 2014). In between these chron boundaries, we use linear interpolation to transfer the XRF and stable isotope depth-series into time-series. Benthic stable isotope data are given in Supplementary Table 4.

2.3. Analytical methods for stable isotopes of benthic foraminifera

Sediment samples were soaked in sodium metaphosphate (according to a cleaning protocol for Eocene Exp. 342 samples; Hull et al., 2017) and washed through a 150 µm sieve. Based on availability, 5–15 well preserved, 'glassy' (*sensu* Sexton et al., 2006b) specimens of the benthic foraminifera *Nuttallides truempyi* without any visible infillings were picked from the >150 µm fraction in order to generate stable carbon and oxygen isotope data. These 'glassy' foraminifera contrast sharply with the 'frosty' preservation (Sexton et al., 2006b) that is typical of fossil foraminifera from the vast majority of deep-sea sedimentary sequences. Samples were measured on a Finnigan MAT 251 gas isotope ratio mass spectrometer connected to a Kiel III automated carbonate preparation device at MARUM, Bremen. Data are reported in the usual delta-notation versus V-PDB. The instrument was calibrated against the in-house standard (ground Solnhofen limestone), which in turn was calibrated against the NBS-19 standard reference material. Over the measurement period the standard deviations of the in-house standard were 0.03‰ for δ^{13}C and 0.07‰ for δ^{18}O. Benthic foraminiferal carbon and oxygen isotopes from *Nuttallides truempyi* were corrected to *Cibicidoides* using well established interspecies correction factors (Katz et al., 2003). We plot and discuss all benthic foraminiferal isotope data corrected to *Cibicidoides*.

2.4. Time-series analysis

Time-series analysis was carried out using the REDFIT algorithm (Schulz and Mudelsee, 2002) for unevenly spaced time series as implemented in the PAST software (Hammer et al., 2001). The analyses were performed in the time-domain with a Welch-window and without oversampling or segmentation. Prior to spectral analyses a *Lowess* smoother (smoothing factor = 0.66 equal to ~1.7 Myr) was applied to all data series to remove long-term trends. Bandpass filters isolate and extract the components of

signals associated with a specific range of frequencies. We employed band-pass filters to assess the behaviour of a specific range of frequencies in a studied signal using the R astrochron package (Meyers, 2014). The periodicity range for bandpass filtering of obliquity cycles is between 29 and 55 kyr. We chose such a relatively broad range in order to capture the major obliquity components at 41 kyr, 54 kyr and 29 kyr (Laskar et al., 2004), which is crucial for a correct representation of amplitude modulation patterns. We obtained the amplitude envelope of the obliquity-filtered signal by the application of the Hilbert Transform, as implemented in astrochron. A lowpass filter at 130 kyr was applied to the obliquity amplitude modulation to capture the main obliquity amplitude modulation periods. The frequency range for the direct 173-kyr filter is between 130 and 220 kyr. Phase estimates and coherences were calculated with the Blackman-Tukey method using the *Analyseries* software (Paillard et al., 1996).

2.5. Earth system model

Eocene climate simulations were performed using the Earth system model *COSMOS*, in the coupled atmosphere-ocean configuration with prescribed vegetation. The model configuration includes the atmosphere component ECHAM5 at T31/L19 resolution, i.e. a horizontal resolution of ~3.75° with nineteen vertical layers (Roeckner et al., 2006). The Max Planck Institute Ocean Model (MPI-OM) runs in a GR30/L40 configuration, i.e. has an average horizontal resolution of 3° × 1.8° with 40 uneven vertical layers (Marsland et al., 2003). MPI-OM includes the dynamics of sea ice formulated using viscous-plastic rheology (Hibler III, 1979). Our version of *COSMOS* has been extensively used and validated in the context of glacial (Werner et al., 2016; Zhang et al., 2014), interglacial (Lohmann et al., 2013; Pfeiffer and Lohmann, 2016), and Miocene (Knorr et al., 2011; Knorr and Lohmann, 2014) climates.

In order to model deep-water circulation at and after the early-middle Eocene boundary, we employed an Ypresian (56–47.8 Ma) paleogeography compiled by GETECH (Lunt et al., 2016) and modified the paleogeography in the North Atlantic to account for the tectonic changes at the early-middle Eocene boundary. We have modified the original paleogeography by closing the Gibraltar Straits following the reconstruction by Stampfli et al. (2002). A deep connection between the Greenland-Norwegian Sea and the North Atlantic via the deepest part of the Greenland-Scotland Rift was established by at least ~48.5 Ma (Hohbein et al., 2012). The Arctic Ocean was an isolated, poorly ventilated basin, comparable to the modern Black Sea (Stein et al., 2006) and the Fram Strait only connected the Greenland-Norwegian Sea and the Arctic from the early Miocene onwards (Jakobsson et al., 2007). For this reason, we employ a paleogeography with a closed Fram Strait and a Greenland-Norwegian Sea gateway of 500 m water depth in our obliquity minimum/maximum experiments.

Based on this paleogeography, the boundary conditions to run the model include the prescription of vegetation distribution (Sewall et al., 2007), the set-up of the hydrological discharge model (Hagemann and Dümenil, 1997), orography-related parameters for the gravity wave drag parameterization (Lott and Miller, 1997), glacier mask, the concentration of greenhouse gases in the atmosphere, and orbital parameters. The solar constant was reduced by 0.6% compared to present-day and is equal to 1358.8 W/m^2. Eccentricity and precession were set to present day values. The CO_2 level was set to 3x pre-industrial level (840 ppm) (Anagnostou et al., 2016), while other greenhouse gases were set to present day values. We prescribed no ice sheets in either hemisphere.

We set up two experiments, with different obliquity angles, keeping eccentricity and precession constant. In the first experiment (OBL$_{MIN}$), obliquity is set to a minimum value of 22.1°, while in the second (OBL$_{MAX}$) to a maximum value of 24.5°. Both sim-
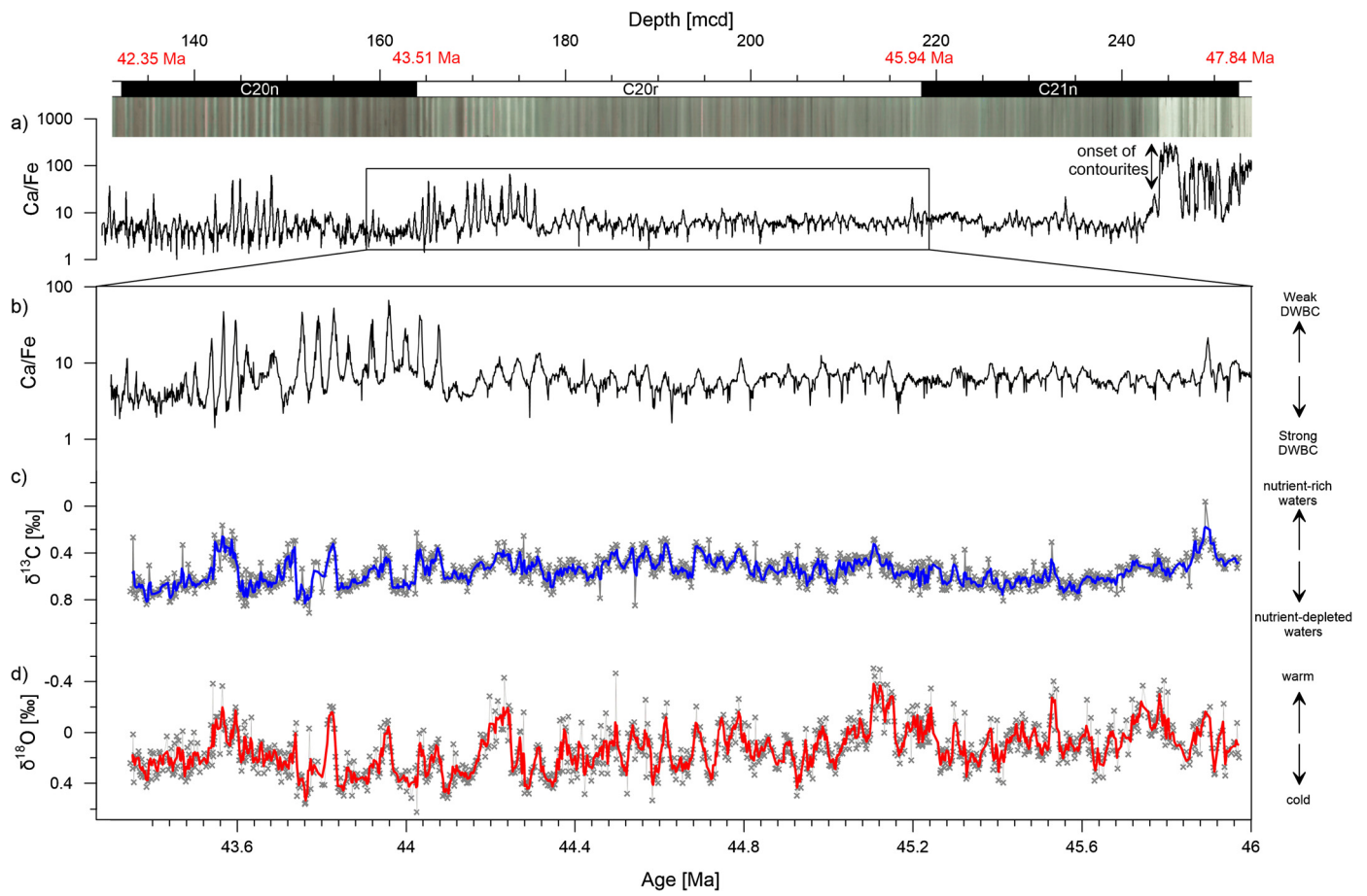
Fig. 2. Obliquity-paced paleoceanographic proxy records from IODP Site U1410. (a) XRF-derived Ca/Fe indicate the onset of drift sedimentation at 244 mcd. (b–d) Ca/Fe, $\delta^{13}C_{benthic}$ and $\delta^{18}O_{benthic}$ records of chron C20r in the time domain. We consider C20r boundary ages of 43.51 and 45.94 Ma and apply linear interpolation in between these tie-points, so to convert depth into time. Blue and Red lines on the isotopic curves represent the 6-kyr running averages. (For interpretation of the references to colour in this figure legend, the reader is referred to the web version of this article.)

ulations were integrated for 7000 model years to reach steady state. The analysis is based on a climatology (long-term average) calculated from the last 100 years of simulations. We run an additional minimum obliquity experiment with an adjusted Greenland-Scotland Ridge sill depth of 200 m to test the sensitivity of NCW formation to this bathymetric feature. The simulation was restarted from experiment OBL_{MIN} at a model year 6200 and was further run for 800 years to the model year 7000.

3. Results

3.1. Paleoceanographic proxies and their astronomical interpretation

Cyclic drift deposits replace continuous pelagic sediment at 244 mcd within the deeper third of chron C21n. The investigated sediment section (~158–219 mcd) in chron C20r contains middle Eocene sediment drift deposits composed of light grayish green nannofossil clay interlayered with nannofossil ooze. These well-developed alternations between nannofossil clay and nannofossil ooze reflect the primary lithological cycles in carbonate content. Carbonate content varies between ~30 wt% in the darker nannofossil clay and 80 wt% in the nannofossil ooze (Boyle et al., 2017; Norris et al., 2014). The alternation between both lithologies is well captured by the XRF-derived ratio between calcium and iron (Ca/Fe), with high Ca/Fe ratios in the nannofossil ooze and low ratios in the clay-rich intervals. The onset of the drift sediments is marked by a sharp decrease in the mean Ca/Fe ratio at 244 mcd (Fig. 2a).

3.1.1. XRF-derived Ca/Fe

The Ca/Fe ratio in chron C20r is characterized by low amplitude cycles of less than 10 counts/counts in the older part of the chron (46–44.1 Ma) and high amplitude of up to 80 counts/counts in its younger part (44.1–43.5 Ma). The power spectrum of the log(Ca/Fe) time-series suggest obliquity as the main driver of Ca/Fe variance, as it exhibits a double spectral peak exceeding the 99% confidence level (CL) at obliquity-related periods of 29–55 kyrs (between 0.018–0.034 cycles/kyr; Fig. 3a).

Another strong spectral peak emerges at a period of 18.7 kyr (0.053 cycles/kyr), very close to the frequency where one would expect the imprint of the ~20-kyr precession cycle. However, this spectral peak is more likely to be the first harmonic of the fundamental frequency of the obliquity cycles. Indeed, the log(Ca/Fe) cycles are characterized by a non-sinusoidal periodic waveform (Supplementary Fig. 2a). Using Fourier expansion, such a signal is represented by the sum of an infinite series of all-integer harmonic frequencies. This means that a power spectrum of such a signal will have a harmonic peak at all multiples of the fundamental frequency, in this case obliquity (Supplementary Fig. 2b). Hence, we interpret the observed peak at 18.7 kyr as the first harmonic of obliquity, rather than as the imprint of precession. Apparent amplitude modulations of obliquity with a frequency of ~173 kyr result from the resonance or "beat" between the (present-day) 41-kyr and 53-kyr obliquity cycles, for which the frequencies are determined by the precession constant and the frequency of the ascending node precession of respectively the Earth–Moon body ($p+s_3$) and Saturn ($p+s_6$) (Laskar et al., 2004).
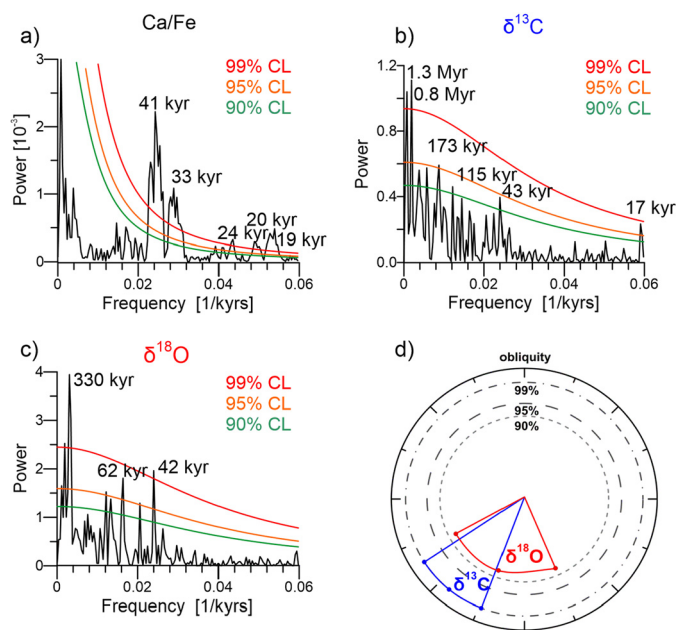
Fig. 3. Spectral and phase analysis of proxy records. Redfit power spectra of the a) Ca/Fe, b) $\delta^{13}C_{benthic}$, and c) $\delta^{18}O_{benthic}$. Main periods are highlighted. d) Phase wheel illustrating the phase relations between benthic foraminiferal stable isotopes and Ca/Fe at the obliquity band (41 kyr). In the phase wheel representation, vectors in the 12 o'clock position are in phase with maximum Ca/Fe, and phase lags increase in the clockwise direction (for example, 3 o'clock represents a 90° lag relative to Ca/Fe, 6 o'clock represents an antiphase response, and 9 o'clock represents a 90° lead). Vector length (from circle centre to middle of arc) represents coherence, and the associated arc denotes the phase within 2σ phase error. Circles mark 99% (dashed-dotted), 95% (dashed) and 90% (dotted) coherence.

3.1.2. Benthic foraminiferal carbon isotopes

Our benthic foraminiferal isotope record consists of 1185 measurements between 43.35–46 Ma. Benthic carbon isotopes in chron C20r range between −0.04‰ and 0.91‰. Peaks exceeding the 95% confidence level in the power spectrum of $\delta^{13}C$ appear at frequencies related to short eccentricity (∼0.086 cycles/kyr) and precession (0.058 cycles/kyr), while a peak close to the 95% confidence level occurs at the frequency of obliquity (43 kyr) (Fig. 3b). Other significant peaks at frequencies of 1.29 Myr (0.00078 cycles/kyr) and 173 kyr (0.0058 cycles/kyr) are at the timescale of the long-term response of the carbon cycle to the 1.2 Myr and the 173-kyr obliquity amplitude modulation, while another significant peak appears at a frequency of 800 kyr. The carbon isotope record thus seems to be characterized by short and long-term orbital variability superimposed on a low amplitude increase of 0.02‰/Myr throughout chron C20r.

3.1.3. Benthic foraminiferal oxygen isotopes

Benthic foraminiferal oxygen isotope values range between −0.51‰ and 0.62‰ and follow the previously-observed general cooling trend in benthic foraminiferal oxygen stable isotopes throughout the middle Eocene (Cramer et al., 2009). In our record, this increase amounts to 0.11‰/Myr throughout chron C20r. Significant peaks in the power spectrum of benthic $\delta^{18}O$ occur at 42 kyr (0.024 cycles/kyr) and at ∼330 kyr (0.003 cycles/kyr), close to the periods of obliquity (41 kyr) and possibly related to long eccentricity (405 kyr) (Fig. 3c).

3.1.4. Proxy phase relationship

The fit between observed frequencies and expected orbital frequencies in all three proxy records is remarkable given the fact that the age model is based on linear interpolation between the chron boundaries rather than on astronomical tuning and thus prevents circular reasoning by introducing power into expected orbital

frequencies. The records of benthic foraminiferal $\delta^{13}C$ and $\delta^{18}O$ are in phase (i.e. positively correlated). Minima in $\delta^{13}C$ correspond to minima in $\delta^{18}O$ and vice versa. On the other hand, benthic foraminiferal isotopes are in antiphase (i.e. negatively correlated) with log (Ca/Fe). Minima in $\delta^{13}C$ and $\delta^{18}O$ lead maxima in log (Ca/Fe) by ∼4.5 kyr and ∼2.5 kyr, and vice versa. The coherence between $\delta^{13}C$ and Ca/Fe exceeds the 99% CL and thus indicates a very stable phase difference between the two proxy records.

3.2. Earth system model

Figs. 4a and 4d display global SSTs, as simulated by the Earth system model, under minimum and maximum obliquity conditions, respectively. On average, SSTs are 1.5 °C cooler during obliquity minima relative to obliquity maxima (Fig. 4g). The average deep-water temperature difference between both astronomical configurations is 0.2 °C, with the obliquity minimum simulation being cooler than the obliquity maximum simulation. The amount of relative cooling gradually increases towards the poles; the Arctic is characterized by a 5.9 °C difference between both simulations. The latitudinal SST gradient increases by 5.5 °C during obliquity minima compared to obliquity maxima, a feature seen in other models (Mantsis et al., 2011).

Deep-water cooling of up to 1.3 °C occurs during obliquity minima in the Arctic Ocean, the North Atlantic and the Nordic Sea. The model predicts that Site U1410 was exposed to ∼1.2 °C cooler bottom waters during middle Eocene obliquity minima compared to obliquity maxima (Fig. 5).

Average global sea surface salinities (SSS) are 0.4 psu higher during obliquity minima compared to obliquity maxima. Differences are most pronounced in the Tethys, where surface salinities increase by more than 2 psu during obliquity minima (Figs. 4b, 4e and 4h). At the same time, SSS decreases by ∼0.5 psu in the Labrador Sea, while SSS in the Greenland-Norwegian Sea is barely affected by variations in obliquity.

The simulated deep-water formation is strongly seasonal and occurs primarily in the Weddell Sea and Ross Sea during boreal summer and in the Eastern North Atlantic and the Greenland-Norwegian Sea during boreal winter. Mixed-layer depth is deeper during obliquity minima in boreal winter in the Greenland-Norwegian Sea (Figs. 4c, 4f and 4i). Deep Western Boundary Currents at the paleodepth of Site U1410 (∼2950 m) are faster during obliquity minima, while during obliquity maxima stronger currents occur in intermediate water depth ∼1500 m.

Our simulations exhibit deep-water formation and a Deep Western Boundary Current in the North Atlantic in all three simulations (Fig. 6), indicated also in the global meridional ocean circulation. Enhanced overturning with depth down to 4200 m is detected for minimum obliquity, whereas a reduced overturning with depths down to 3500 m is detected for maximum obliquity, and for the model set up with minimum obliquity and assuming a 200 m sill depth of the Greenland-Scotland Ridge (Fig. 6).

The simulation with the shallower Greenland-Scotland Ridge sill depth shows that the exact geometry of NCW and SCW is susceptible to changes in the overflow capacity out of the Greenland-Norwegian Sea. The deep-water formation is weaker and shallower in the shallow sill simulation compared to simulations with a 500 m deep Greenland-Scotland Ridge, while the Southern Ocean component is strengthened.

4. Discussion

In this section, we will use the results from our paleoclimate simulation experiments to illustrate the mechanism involved in the invigoration of NCW formation in response to orbital forcing. It should be noted, however, that the exact amplitude of
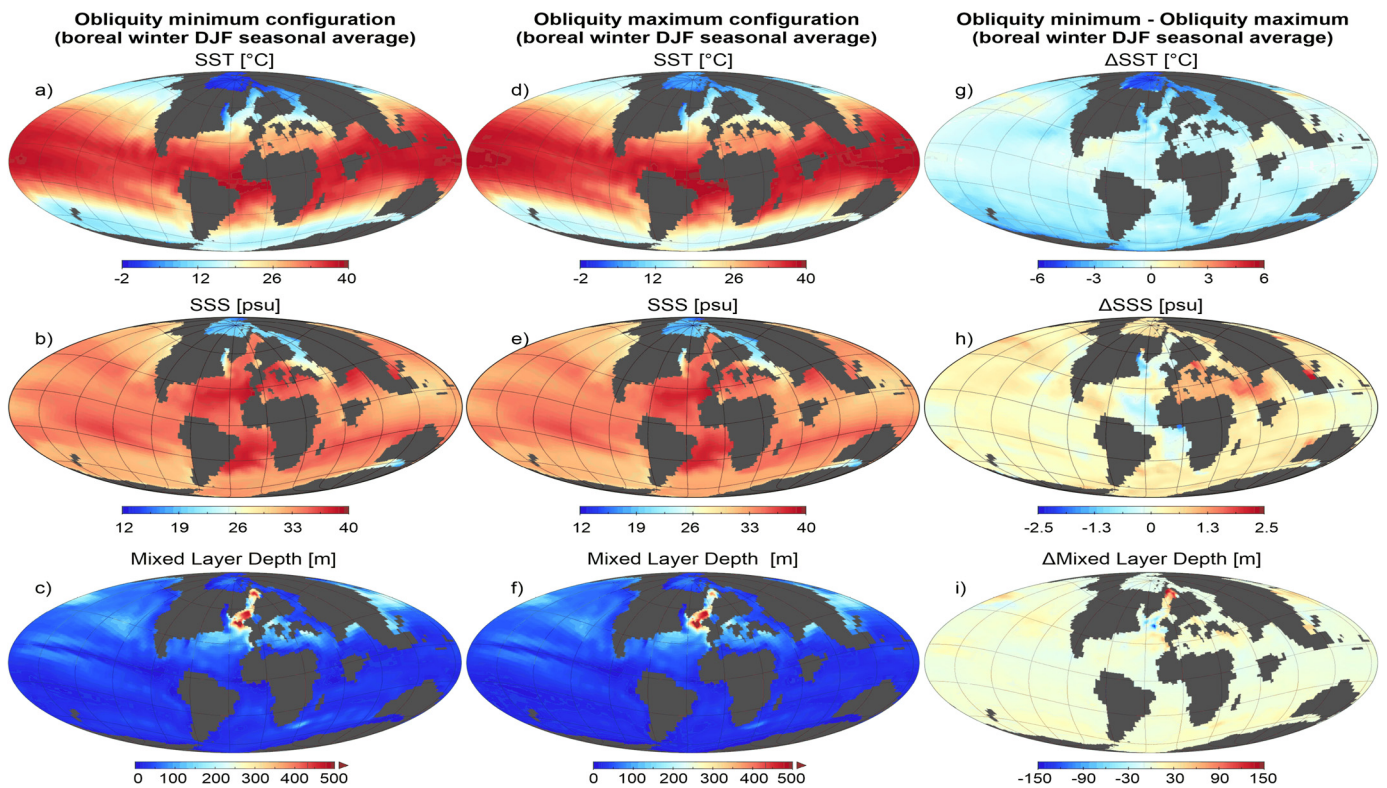
Fig. 4. Boreal winter paleoceanography as simulated by the *COSMOS* model. Seasonally averaged Sea Surface Temperature (SST), Sea Surface Salinity (SSS) and mixed layer depth for boreal winter under (a–c) obliquity minimum configuration, and under (d–f) obliquity maximum configuration. (g–i) Seasonal differences in SST, SSS and mixed layer depth between the obliquity minimum and obliquity maximum simulations.
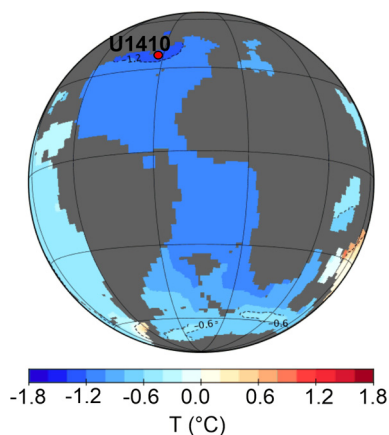

Fig. 5. Annual difference in temperature at 2785 m water depth between the obliquity minimum and the obliquity maximum simulation. The depth of 2785 m corresponds to the approximate paleodepth of Site U1410 during the middle Eocene.

astronomically-forced change depends on different boundary conditions (e.g. paleobathymetry, atmospheric CO$_2$ level, vegetation distribution, continental ice volume).

4.1. Paleoceanographic change in the Western North Atlantic

Proxy records at Site U1410 in the Western North Atlantic off Newfoundland reveal a strong imprint of obliquity. However, during the middle Eocene, Site U1410 was located at a paleolatitude of ∼41°N, where 83% of the variability in incoming summer insolation (June 21) is ascribed to precession and only 17% to obliquity (relative amplitude of obliquity compared to precession at 41°N over the past 1 Ma from Laskar et al., 2004). In that respect, it is remarkable that the log (Ca/Fe) and stable isotope proxy records

exhibit an astronomical imprint that is dominated by obliquity. The most likely explanation for this observation is an oceanographic teleconnection between the paleolocation of Site U1410 and high latitudes, where obliquity has its maximum influence on insolation variability.

A mechanism to enable such an oceanographic teleconnection is the invigoration of Deep Western Boundary Currents in response to the onset of NCW formation, which has previously been linked to the deposition of contourite drift sediments at the early-middle Eocene boundary across the North Atlantic (Boyle et al., 2017; Hohbein et al., 2012). At Site U1410, this change in bottom water circulation is marked by the sharp decrease in Ca/Fe at ∼47 Ma coinciding with a lithology change from biogenic pelagic sediments to muddy drift sediments. Several lines of evidence imply that the lithological variability in carbonate content is related to the input of clay: (1) Middle Eocene carbonate deposition between ∼3300 and ∼4300 m paleo-water depth at IODP Expedition 342 sites indicate a deep North Atlantic carbonate compensation depth (CCD) at this time (Norris et al., 2014), with the CCD lying well below the paleodepth of Site U1410. The excellent preservation of calcareous microfossils at Site U1410 further strengthens these observations. (2) An order-of-magnitude increase in bulk sediment mass accumulation rates, due primarily to an increase in the terrigenous component (Boyle et al., 2017). (3) Increases in the sedimentation rate at Site U1410 with the onset of drift sediments have the same proportional magnitude as decreases in CaCO$_3$ content at the same time (Norris et al., 2014). These arguments together exclude changes in productivity as the primary driver of the Ca/Fe signal. In contourite deposits, winnowing and sorting of particles of different grain-size and specific weight should have a significant influence the grain size and elemental composition. At flow speeds below 10–15 cm s^{-1} common for the deposition of muddy contourites, sediment composition is controlled by selective deposition, whereas winnowing and erosion only play a role at faster cur-
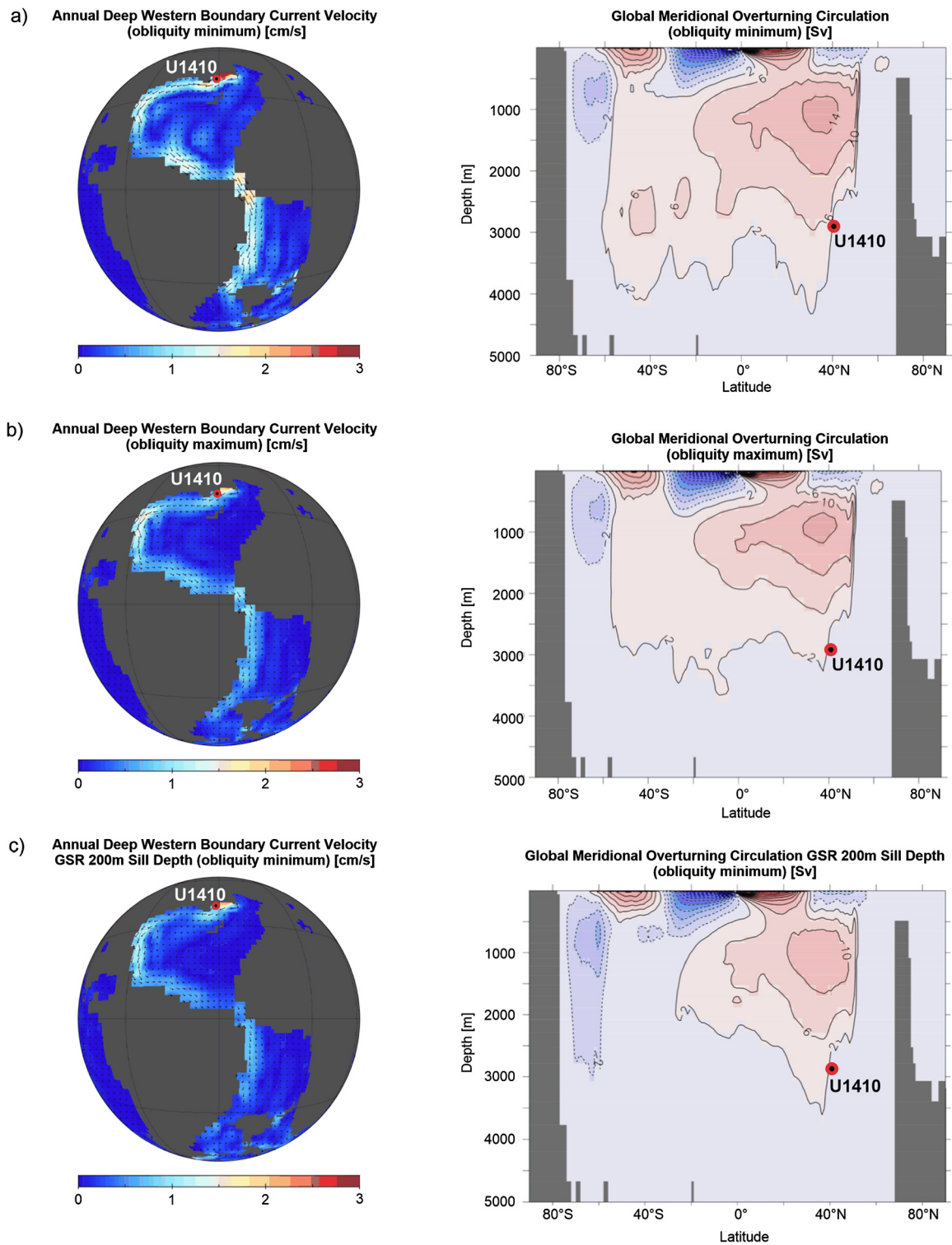
Fig. 6. Deep western boundary current velocity and global meridional overturning circulation. Annually averaged current velocities during (a) the obliquity minimum and (b) the obliquity maximum simulation. (c) Annually averaged current velocities under a minimum obliquity configuration and for a Greenland-Scotland Ridge 200 m sill depth (500 m in nominal simulations in panels (a–b)). Positive values (red) indicate clockwise overturning cells; negative values (blue) indicate counter-clockwise overturning cells. The contour spacing is 4 Sverdrup. (For interpretation of the references to colour in this figure legend, the reader is referred to the web version of this article.)
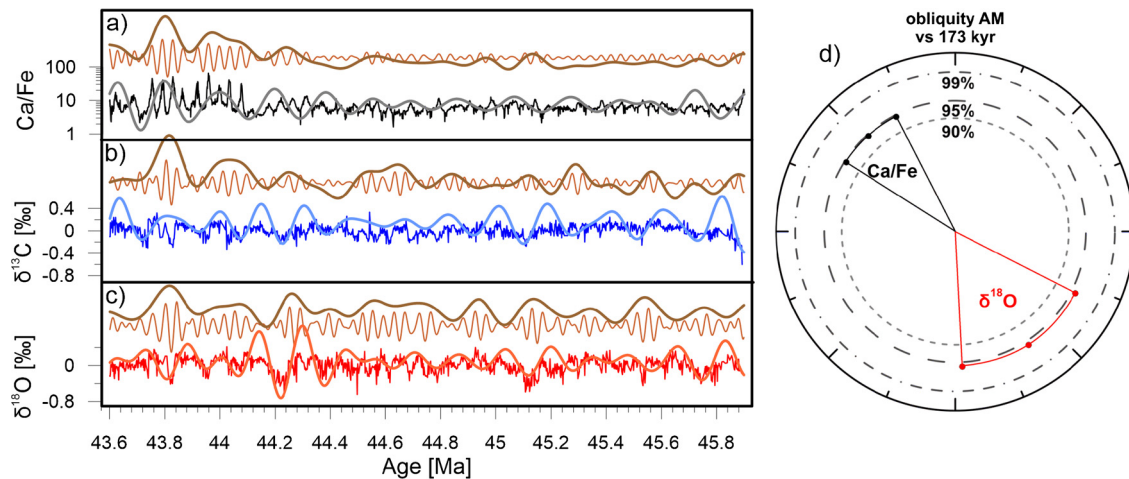
Fig. 7. The 173-kyr cycle in the amplitude modulation of obliquity. The amplitude envelope (light brown) of the obliquity band-pass filtered signal (brown) generally exhibits an in-phase relation with the direct 173-kyr band-pass filtered signal, as extracted from the (a) Ca/Fe (black/grey), (b) $\delta^{13}C_{benthic}$ (blue), (c) $\delta^{18}O_{benthic}$ (red). Phase wheel (d) illustrating the phase relations between benthic foraminiferal stable oxygen isotopes (red) and Ca/Fe (black) at the obliquity amplitude modulation band (173 kyr). In the phase wheel representation, vectors in the 12 o'clock position are in phase with maximum Ca/Fe, and phase lags increase in the clockwise direction (for example, 3 o'clock represents a 90° lag relative to Ca/Fe, 6 o'clock represents an antiphase response, and 9 o'clock represents a 90° lead). Vector length (from circle centre to middle of arc) represents coherence, and the associated arc denotes the phase within 2σ phase error. (For interpretation of the references to colour in this figure legend, the reader is referred to the web version of this article.)

rent velocities (McCave and Hall, 2006). The increase in terrigenous accumulation and the drop in the ratio of Ca/Fe at the onset of the drifts indicates that current velocities were sufficient to transport clay from sources along the northeast Canadian continental margin southward to the topographically isolated Newfoundland ridges but insufficient for winnowing (Boyle et al., 2017). For this reason, we attribute the terrigenous component of the sediment reflected by the ratio of Ca/Fe as a proxy for the Deep Western Boundary Current velocity. Consequently, low Ca/Fe corresponds to strong Deep Western Boundary Currents and vice versa.

Benthic foraminiferal carbon isotope ratios are primarily controlled by deep-water nutrient availability. Modern NADW is a young deep-water mass formed by convection of surface waters predominantly sourced from low latitude areas marked by low nutrient and high chlorophyll where intense phytoplankton productivity effectively strips most of the available nutrients out of surface waters. As such, NADW is relatively nutrient-depleted. Plankton preferentially extracts ^{12}C from surface waters. Young deep-water masses (i.e. close to their source region) forming in regions supplied by surface waters sourced from low latitude areas marked by low nutrients and high chlorophyll are thus enriched in ^{13}C and can be distinguished by their relatively high $\delta^{13}C$ values (Kroopnick, 1985). Alternatively, the changes in benthic foraminiferal carbon isotopes could reflect global changes in $\delta^{13}C_{DIC}$ due to the growth and decay of the terrigenous and geological carbon reservoirs (e.g. terrestrial biosphere, gas hydrates, volcanic outgassing, organic matter accumulation) on obliquity timescales. The phase relation between our proxies (Fig. 3d) reveals that the invigoration of Deep Western Boundary Currents (Ca/Fe minima) corresponds to a greater influence of nutrient-depleted bottom waters and/or the growth of ^{13}C-depleted reservoirs ($\delta^{13}C$ maxima) and cold bottom water temperatures ($\delta^{18}O$ maxima) at Site U1410 on obliquity timescales. The strong coherence between Ca/Fe and $\delta^{13}C$ (Fig. 3) supports a common mechanism driving both proxies, related to NCW variability in the western North Atlantic at the rhythm of obliquity.

We propose that episodes of strong NCW formation correspond to obliquity minima based on the following arguments: (1) The phase relationship between obliquity amplitude modulation patterns and a direct 173-kyr filter exhibit a positive phase relationship for Ca/Fe (Fig. 7) and negative phase relationships for $\delta^{18}O$.

These phase relationships indicate that increased Ca/Fe ratios correspond to high variability in Ca/Fe. Thus, we can link high Ca/Fe to obliquity maxima. In the benthic foraminiferal $\delta^{18}O$ record, the direct 173-kyr filter and the obliquity amplitude modulation are in antiphase, linking high obliquity-variability in $\delta^{18}O$ (during a 173-kyr obliquity maximum) with low $\delta^{18}O$. In other words, minima in benthic foraminiferal stable oxygen isotopes correspond to maxima in obliquity. However, the phase analysis between the 173-kyr $\delta^{13}C$ filter and the $\delta^{13}C$ obliquity envelope did not yield results that were statistically significant. Nevertheless, we infer the same obliquity phase relationship for $\delta^{13}C$ as for $\delta^{18}O$, as both are in phase with each other (and in antiphase with Ca/Fe). (2) $\delta^{18}O$ maxima in the deep ocean are generally linked to global cooling in response to obliquity minima (De Vleeschouwer et al., 2017; Hays et al., 1976). (3) Our simulations in *COSMOS* show the same proportional cooling and invigoration of Deep Western Boundary Currents during obliquity minima that we see in our data, providing independent support for the phasing of our data with respect to axial obliquity.

The amplitude of benthic foraminiferal oxygen isotope variability at the 41 kyr rhythm of obliquity ranges between 0.2 and 0.4‰. Using the equation from Bemis et al. (1998), this variability corresponds to deep-water temperature changes between 0.8 and 1.6 °C over the course of a middle Eocene obliquity cycle. These values are in excellent agreement with the results from our climate simulations, which exhibit a 1.2 °C difference between the obliquity minimum and obliquity maximum simulation in the deep northwestern Atlantic (Fig. 5).

In accordance with our paleoceanographic proxy data, our ocean circulation simulations indicate that Deep Western Boundary Currents were invigorated during obliquity minima, transporting more clay to the Newfoundland Ridge than during obliquity maxima (Fig. 6). These simulations also predict a larger amount of nutrient-depleted NCW reached the Newfoundland region during obliquity minima (Fig. 6a, b).

4.2. Source and formation of middle Eocene northern component water

The modern AMOC is characterized by overturning cells in the Southern Ocean (Antarctic Bottom Water) and in the North Atlantic (NADW). The two major components of modern NADW are Nordic
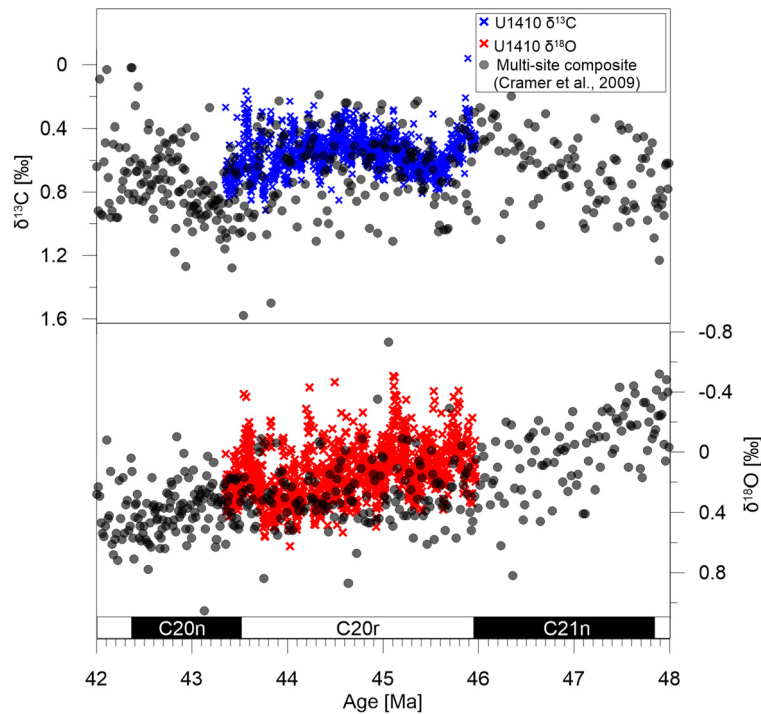
Fig. 8. Global benthic foraminiferal isotope composite (black) plotted against δ^{13}C (blue) and δ^{18}O (red) from site U1410. U1410 *N. truempyi data* are corrected to *Cibicidoides* using correction factors for δ^{13}C (Nut+0.34‰) and δ^{18}O ((Nut+0.10)/0.89) from Katz et al. (2003). (For interpretation of the references to colour in this figure legend, the reader is referred to the web version of this article.)

Sea Overflow Water and Labrador Sea Water. Nordic Sea Overflow Water is the densest part of NADW and is formed through convection of highly saline surface water in the Greenland-Norwegian Sea induced by cooling. Nordic Sea Overflow Water is fed back into the North Atlantic by overflow over the Greenland-Scotland Ridge and forms the lower part of the Deep Western Boundary Current. Labrador Sea Water, on the other hand, is less dense than Nordic Sea Overflow Water and forms the upper part of the Western Boundary Current after convection in the Labrador Sea (Hansen and Østerhus, 2000). Our proxy data do not allow us to distinguish between deep waters convected in the Greenland-Norwegian Sea versus Labrador Sea during the middle Eocene. Yet, several lines of evidence suggest the Greenland-Norwegian Sea as the (primary) source of NCW in the middle Eocene: First, the paleodepth of Site U1410 is ~3000 m, much deeper than the convection depth of modern Labrador Sea Water (Pickart et al., 2002). Second, the onset of drift sedimentation at the Judd Falls Drift on the Greenland-Scotland Ridge suggests deep-water formation in the Greenland-Norwegian Sea in the early middle Eocene (Hohbein et al., 2012). At the same time, the residual depth of the Iceland plume decreased by up to 400 m (Parnell-Turner et al., 2014). As the residual depth of the Iceland Plume was robustly linked to the percentage of NCW for the last 10 Ma (Poore et al., 2006), the low residual depth during the middle Eocene could have enabled first considerable NCW overflow over the GSR. Third, our modelling results show the Eastern North Atlantic and the Greenland-Norwegian Sea as the primary overturning locations during boreal summer, while no deep-water formation occurs in the Labrador Sea.

A later onset of Labrador Sea Water in the late Eocene to early Oligocene is in agreement with previous studies (Borrelli et al., 2014; Kaminski et al., 1989). Based on the available paleoceanographic evidence, we propose the onset of NCW in the Greenland-Norwegian Sea at the early-middle Eocene boundary and a later initiation of deep-water formation in the Labrador Sea.

4.3. The role of Northern Component Water in the evolution of global climate

Inter-basinal benthic δ^{13}C and δ^{18}O gradients are commonly used to distinguish between different water masses. Cramer et al. (2009) used a global compilation of benthic isotope records to assess Cenozoic paleocenaographic change, whereas Sexton et al. (2006a) focused on the Eocene. These authors show that Paleogene δ^{13}C signatures of deep waters were very similar between the different ocean basins, particularly between the North Atlantic and the South Atlantic. The U1410 benthic δ^{13}C values during the middle Eocene are on the lower range of the global composite and in the same range with previous values from the North Atlantic. Middle Eocene North Atlantic δ^{13}C values are intermediate between, but very similar to those of the South Atlantic and the Southern Ocean. Accordingly, interbasinal benthic δ^{13}C was low to non-existent, until Pacific benthic δ^{13}C started to become lighter from about 14 Ma onwards, whereas the Southern Ocean demonstrates a trend towards lighter values from about 8 Ma. Together, this suggests that inter-basinal δ^{13}C gradients may not have been as useful as a water mass tracer as in the modern ocean and have been modulated by additional mechanisms such as the link between climate and the biological productivity. This is supported by the correspondence between δ^{13}C and δ^{18}O during the middle Eocene.

Benthic foraminiferal δ^{18}O gradients have been used to track the onset of the modern bimodal ocean circulation based on thermal differentiation between the ocean basins. Studies based on this proxy for thermal differentiation between the North Atlantic and the Southern Ocean suggest the onset of NCW at 38.5 Ma, yet do not preclude an earlier contribution from GSR overflow (Borrelli et al., 2014; Langton et al., 2016). However, this date is unsupported by evidence from other proxies such as the onset of North Atlantic drift sedimentation and Nd isotopes. Just as for the carbon isotopes, our benthic foraminiferal oxygen isotopes are in the range of existing global benthic foraminiferal isotope values for the middle

Eocene (Fig. 8). The U1410 benthic $\delta^{18}O$ values are at the low end (i.e., warmer/less salty) of the global stack, reflecting the warming of the Atlantic and the Southern Ocean relative to the Pacific, which starts at ∼48 Ma (Cramer et al., 2009). The relative warming of the Atlantic with respect to the Pacific can be explained by the onset of convection in the North Atlantic and thus the increased export of energy from the surface to the deep North Atlantic. We therefore propose that further thermal differentiation between Atlantic water masses occurred as a result of cooling in the deep Southern Ocean rather than the onset of NCW at 38.5 Ma. Such cooling has been shown to result from the opening of the Drake and Tasman Passages and the establishment of the proto-Antarctic Circumpolar Current during this time (Sijp et al., 2011). We thus infer a more complicated and variable history of deep-water circulation in the Atlantic between the onset of the Cenozoic cooling at ∼49 Ma and the large scale glaciation of Antarctica at the Eocene–Oligocene boundary.

4.4. Response of NCW production to astronomical forcing

NCW formation in the Greenland-Norwegian Sea is driven by the density gradient between the surface ocean and underlying water layers. This density gradient responds sensitively to changes in the salt balance and temperatures at the North Atlantic convection sites. We propose a combination of five different climatic feedback mechanisms, responding to astronomical forcing, explaining the strong NCW signal during obliquity minima in sediments from the Newfoundland Ridge.

Cooler global temperatures during obliquity minima, amplified in the North Atlantic, result in enhanced oceanic heat loss to the atmosphere in the North Atlantic. The strong cooling increases the density of the saline surface waters flowing north from the subtropics. This process could increase surface water density until that water starts to sink.

Moreover, during obliquity minima, comparatively weak insolation at high latitudes cools the water (density increases), while the stronger than normal insolation at low latitudes induces warmer water (density decreases). The resulting enhanced meridional density gradient favours a stronger overturning (Butler et al., 2016). Interestingly, the occurrence of ice rafted debris indicates the initiation of glaciation around the Arctic and the Greenland-Norwegian Sea around the same time as the initiation of NCW at ∼47 Ma and ∼44 Ma, respectively (Stickley et al., 2009; Tripati et al., 2008). Because lower obliquity decreases annual-average insolation at high latitudes, sea ice growth should peak during localized cold periods coeval with obliquity minima. Sea-ice formation removes freshwater from the ocean, leaving behind enough salt to increase the salinity of the upper ∼25 m of the water column by 1 psu per meter of sea ice thickness (Maykut, 1985).

A decline in seasonality owing to low obliquity weakens the hydrological cycle in the Northern Hemisphere and preferentially decreases total annual precipitation across the high latitudes (Lawrence et al., 2003). The resulting reduction of freshwater influx into the Greenland-Norwegian Sea and the North Atlantic would increase the density of surface waters, thereby strengthening thermohaline circulation.

The observed changes in North Atlantic circulation in our proxy data could result from changes in atmospheric CO_2 responding to variations in obliquity. In the geological record and climate models, elevated deep-sea temperatures (De Vleeschouwer et al., 2017; Hays et al., 1976) and higher atmospheric CO_2 concentrations (Scheffer et al., 2006) correspond to obliquity maxima (Lüthi et al., 2008). Global warming and elevated atmospheric CO_2 can weaken the thermohaline circulation by surface water warming and surface water freshening (Rahmstorf, 2006). Consequently, increasing atmospheric CO_2 concentration during obliquity maxima has the

potential weaken NCW formation by decreasing the density of the surface water.

In our middle Eocene simulations, SST in the North Atlantic and Greenland-Norwegian Sea respond sensitively to changes in obliquity, while little variance in SSS in these regions suggests only a minor impact of the hydrological cycle on overturning intensity (Fig. 4b, e, h). Sea ice formation does not occur outside of the Arctic in our middle Eocene simulation, while sedimentological evidence indicates that temperatures were seasonally cold enough to allow the formation of glaciers around the Nordic Seas at ∼44 Ma (Tripati et al., 2008). We therefore conclude that temperatures at the deep-water formation areas and increased vertical and meridional density gradients are the main modulators of middle Eocene overturning intensity. The coherency of $\delta^{13}C$ with $\delta^{18}O$ supports the proposed role of orbital forcing on regional deep-water formation.

5. Conclusions

High-resolution benthic foraminiferal stable oxygen and carbon isotopes from contourite deposits in the western North Atlantic (Newfoundland Drift, IODP Expedition 342, Site U1410) combined with geochemical data from XRF reflect bottom water nutrient-content, temperature and Deep Western Boundary Current velocity. Records from the Newfoundland Drifts indicate variations in NCW formation and associated Deep Western Boundary Current strength on orbital timescales, dominated by obliquity. Combined with global circulation model experiments the results show that enhanced overturning is associated with a strong cooling of surface waters in the Greenland-Norwegian Sea during obliquity minima, while NCW formation is weaker with relatively warm temperatures in the Greenland-Norwegian Sea during obliquity maxima. Our modelling results indicate that middle Eocene NCW was primarily formed in the Greenland Norwegian Sea and the eastern North Atlantic.

Appendix A. Supplementary material

Supplementary material related to this article can be found online at https://doi.org/10.1016/j.epsl.2017.12.016.

References

Anagnostou, E., John, E.H., Edgar, K.M., Foster, G.L., Ridgwell, A., Inglis, G.N., Pancost, R.D., Lunt, D.J., Pearson, P.N., 2016. Changing atmospheric CO_2 concentration was the primary driver of early Cenozoic climate. Nature 533, 380–384.

Barron, E.J., Hay, W.W., Thompson, S., 1989. The hydrologic cycle: a major variable during Earth history. Palaeogeogr. Palaeoclimatol. Palaeoecol. 75, 157–174.

Bemis, B.E., Spero, H.J., Bijma, J., Lea, D.W., 1998. Reevaluation of the oxygen isotopic composition of planktonic foraminifera: experimental results and revised paleotemperature equations. Paleoceanography 13, 150–160.

Berggren, W.A., Hollister, C.D., 1974. Paleogeography, paleobiogeography and the history of circulation in the Atlantic Ocean. In: Hay, W.W. (Ed.), Studies in Paleo-Oceanography. In: SEPM Special Publication, vol. 20, pp. 126–186.

Billups, K., Ravelo, A.C., Zachos, J.C., 1997. Early Pliocene deep-water circulation: stable isotope evidence for enhanced northern component deep water. In: Proc. Ocean Drill. Program, Sci. Results, pp. 319–330.

Borrelli, C., Cramer, B.S., Katz, M.E., 2014. Bipolar Atlantic deepwater circulation in the middle–late Eocene: effects of Southern Ocean gateway openings. Paleoceanography 29, 308–327.

Boyle, P.R., Romans, B.W., Tucholke, B.E., Norris, R.D., Swift, S.A., Sexton, P.F., 2017. Cenozoic North Atlantic deep circulation history recorded in contourite drifts, offshore Newfoundland, Canada. Mar. Geol. 385, 185–203.

Broecker, W.S., 1998. Paleocean circulation during the last deglaciation: a bipolar seesaw? Paleoceanography 13, 119–121.

Broecker, W.S., Peng, T.-H., 1982. Tracers in the Sea. Eldigo Press, Lamont-Doherty Geological Observatory, New York.

Butler, E.D., Oliver, K.I.C., Hirschi, J.J.-M., Mecking, J.V., 2016. Reconstructing global overturning from meridional density gradients. Clim. Dyn. 46, 2593–2610.

Cramer, B., Miller, K., Barrett, P., Wright, J., 2011. Late Cretaceous–Neogene trends in deep ocean temperature and continental ice volume: reconciling records of benthic foraminiferal geochemistry (δ^{18}O and Mg/Ca) with sea level history. J. Geophys. Res. 116, C12023.

Cramer, B., Toggweiler, J., Wright, J., Katz, M., Miller, K., 2009. Ocean overturning since the Late Cretaceous: inferences from a new benthic foraminiferal isotope compilation. Paleoceanography 24.

Davies, R., Cartwright, J., Pike, J., Line, C., 2001. Early Oligocene initiation of North Atlantic deep water formation. Nature 410, 917–920.

De Boer, A., Sigman, D., Toggweiler, J., Russell, J., 2007. Effect of global ocean temperature change on deep ocean ventilation. Paleoceanography 22.

De Boer, G.J., Pietrzak, J.D., Winterwerp, J.C., 2008. Using the potential energy anomaly equation to investigate tidal straining and advection of stratification in a region of freshwater influence. Ocean Model. 22, 1–11.

De Vleeschouwer, D., Vahlenkamp, M., Crucifix, M., Pälike, H., 2017. Alternating Southern and Northern Hemisphere climate response to astronomical forcing during the past 35 m.y. Geology 45 (4), 375–378.

Gradstein, F.M., Ogg, J.G., Schmitz, M., Ogg, G., 2012. The Geologic Time Scale 2012. Elsevier.

Hagemann, S., Dümenil, L., 1997. A parametrization of the lateral waterflow for the global scale. Clim. Dyn. 14, 17–31.

Hammer, Ø., Harper, D., Ryan, P., 2001. PAST-palaeontological statistics, ver. 1.89. Palaeontol. Electronica 4.

Hansen, B., Østerhus, S., 2000. North Atlantic–Nordic Seas exchanges. Prog. Oceanogr. 45, 109–208.

Hays, J.D., Imbrie, J., Shackleton, N.J., 1976. Variations in the Earth's orbit: pacemaker of the Ice Ages. Science 194, 1121–1132.

Hibler III, W., 1979. A dynamic thermodynamic sea ice model. J. Phys. Oceanogr. 9, 815–846.

Hohbein, M.W., Sexton, P.F., Cartwright, J.A., 2012. Onset of North Atlantic deep water production coincident with inception of the Cenozoic global cooling trend. Geology 40, 255–258.

Hull, P.M., Bohaty, S.M., Cameron, A., Coxall, H.K., D'haenens, S., De Vleeschouwer, D., Elder, L.E., Friedrich, O., Kerr, K., Turner, S.K., Kordesch, W.E.C., Moriya, K., Norris, R.N., Opdyke, B.N., Penman, D.E., Pälike, H., Wilson, P.A., Sexton, P.F., Vahlenkamp, M., Wu, F., Zachos, J.C., 2017. Data report: coarse fraction record for the Eocene megasplice at IODP Sites U1406, U1408, U1409, and U1411. In: Norris, R.D., Wilson, P.A., Blum, P., the Expedition 342 Scientists (Eds.), Proceedings of the Integrated Ocean Drilling Program, vol. 342. Integrated Ocean Drilling Program, College Station, TX.

Jakobsson, M., Backman, J., Rudels, B., Nycander, J., Frank, M., Mayer, L., Jokat, W., Sangiorgi, F., O'Regan, M., Brinkhuis, H., 2007. The early Miocene onset of a ventilated circulation regime in the Arctic Ocean. Nature 447, 986–990.

Kaminski, M., Gradstein, F., Berggren, W., 1989. Paleogene benthic foraminifer biostratigraphy and paleoecology at site 647, southern Labrador Sea. In: Proceedings of the Ocean Drilling Program: Scientific Results, pp. 705–730.

Katz, M.E., Cramer, B.S., Toggweiler, J., Esmay, G., Liu, C., Miller, K.G., Rosenthal, Y., Wade, B.S., Wright, J.D., 2011. Impact of Antarctic circumpolar current development on late Paleogene ocean structure. Science 332, 1076–1079.

Katz, M.E., Katz, D.R., Wright, J.D., Miller, K.G., Pak, D.K., Shackleton, N.J., Thomas, E., 2003. Early Cenozoic benthic foraminiferal isotopes: species reliability and interspecies correction factors. Paleoceanography 18.

Knorr, G., Butzin, M., Micheels, A., Lohmann, G., 2011. A warm Miocene climate at low atmospheric CO_2 levels. Geophys. Res. Lett. 38.

Knorr, G., Lohmann, G., 2014. Climate warming during Antarctic ice sheet expansion at the Middle Miocene transition. Nat. Geosci. 7, 376–381.

Kroopnick, P., 1985. The distribution of 13C of ΣCO₂ in the world oceans. Deep-Sea Res., A, Oceanogr. Res. Pap. 32, 57–84.

Kuhlbrodt, T., Griesel, A., Montoya, M., Levermann, A., Hofmann, M., Rahmstorf, S., 2007. On the driving processes of the Atlantic meridional overturning circulation. Rev. Geophys. 45.

Kuhlbrodt, T., Rahmstorf, S., Zickfeld, K., Vikebø, F.B., Sundby, S., Hofmann, M., Link, P.M., Bondeau, A., Cramer, W., Jaeger, C., 2009. An integrated assessment of changes in the thermohaline circulation. Clim. Change 96, 489–537.

Langton, S.J., Rabideaux, N.M., Borrelli, C., Katz, M.E., 2016. Southeastern Atlantic deep-water evolution during the late-middle Eocene to earliest Oligocene (Ocean Drilling program site 1263 and Deep Sea Drilling project site 366). Geosphere 12, 1032–1047.

Laskar, J., Robutel, P., Joutel, F., Gastineau, M., Correia, A., Levrard, B., 2004. A long-term numerical solution for the insolation quantities of the Earth. Astron. Astrophys. 428, 261–285.

Lawrence, K., Sloan, L.C., Sewall, J., 2003. Terrestrial climatic response to precessional orbital forcing in the Eocene. Spec. Pap., Geol. Soc. Am., 65–78.

Liu, Z., Herbert, T.D., 2004. High-latitude influence on the eastern equatorial Pacific climate in the early Pleistocene epoch. Nature 427, 720–723.

Lohmann, G., Pfeiffer, M., Laepple, T., Leduc, G., Kim, J.-H., 2013. A model-data comparison of the Holocene global sea surface temperature evolution. Clim. Past 1807–1839.

Lott, F., Miller, M.J., 1997. A new subgrid-scale orographic drag parametrization: its formulation and testing. Q. J. R. Meteorol. Soc. 123, 101–127.

Lunt, D.J., Foster, G.L., O'Brien, C.L., Pancost, R.D., Robinson, S.A., 2016. Palaeogeographic controls on climate and proxy interpretation. Clim. Past 12, 1181–1189.

Lunt, D.J., Ridgwell, A., Sluijs, A., Zachos, J., Hunter, S., Haywood, A., 2011. A model for orbital pacing of methane hydrate destabilization during the Palaeogene. Nat. Geosci. 4, 775–778.

Lüthi, D., Le Floch, M., Bereiter, B., Blunier, T., Barnola, J.-M., Siegenthaler, U., Raynaud, D., Jouzel, J., Fischer, H., Kawamura, K., 2008. High-resolution carbon dioxide concentration record 650,000–800,000 years before present. Nature 453, 379–382.

Mantsis, D.F., Clement, A.C., Broccoli, A.J., Erb, M.P., 2011. Climate feedbacks in response to changes in obliquity. J. Climate 24, 2830–2845.

Marsland, S.J., Haak, H., Jungclaus, J.H., Latif, M., Röske, F., 2003. The Max-Planck-Institute global ocean/sea ice model with orthogonal curvilinear coordinates. Ocean Model. 5, 91–127.

Maykut, G.A., 1985. An Introduction to Ice in the Polar Oceans. DTIC Document.

McCave, I.N., Hall, I.R., 2006. Size sorting in marine muds: processes, pitfalls, and prospects for paleoflow-speed proxies. Geochem. Geophys. Geosyst. 7, Q10N05. https://doi.org/10.1029/2006GC001284.

Meyers, S.R., 2014. Astrochron: AN R Package for Astrochronology http://cran.r-project.org/package=astrochron.

Mosar, J., Eide, E.A., Osmundsen, P.T., Sommaruga, A., Torsvik, T.H., 2002. Greenland–Norway separation: a geodynamic model for the North Atlantic. Norwegian J. Geol., 281–298.

Mulitza, S., Prange, M., Stuut, J.B., Zabel, M., von Dobeneck, T., Itambi, A.C., Nizou, J., Schulz, M., Wefer, G., 2008. Sahel megadroughts triggered by glacial slowdowns of Atlantic meridional overturning. Paleoceanography 23.

Nielsen, S.G., Mar-Gerrison, S., Gannoun, A., LaRowe, D., Klemm, V., Halliday, A.N., Burton, K.W., Hein, J.R., 2009. Thallium isotope evidence for a permanent increase in marine organic carbon export in the early Eocene. Earth Planet. Sci. Lett. 278, 297–307.

Norris, R., Wilson, P., Blum, P., the Expedition 342 Scientists, 2014. In: Proceedings IODP 342. College Station, TX (Integrated Ocean Drilling Program).

Norris, R.D., Kroon, D., Huber, B.T., Erbacher, J., 2001. Cretaceous-Palaeogene ocean and climate change in the subtropical North Atlantic. Geol. Soc. (Lond.) Spec. Publ. 183, 1–22.

Norris, R.D., Wilson, P.A., Blum, P., Fehr, A., Agnini, C., Bornemann, A., Boulila, S., Brown, P.R., Cournede, C., Friedrich, O., Ghosh, A.K., Hollis, C.J., Hull, P.M., Jo, K., Junium, C.K., Kaneko, M., Liebrand, D., Lippert, P.C., Liu, Z., Matsui, H., Moriya, K., Nishi, H., Opdyke, B.N., Penman, D., Romans, B., Scher, H.D., Sexton, P., Takagi, H., Turner, S.K., Whiteside, J.H., Yamaguchi, T., Yamamoto, Y., 2012. Paleogene Newfoundland sediment drifts. In: Integrated Ocean Drilling Program Expedition 342, Prelim Rep. Integrated Ocean Drilling Program Management International, Inc., La Jolla, CA.

Paillard, D., Labeyrie, L., Yiou, P., 1996. Macintosh program performs time-series analysis. Eos, Transactions American Geophysical Union 77, 379.

Pak, D.K., Miller, K.G., 1992. Paleocene to Eocene benthic foraminiferal isotopes and assemblages: implications for deepwater circulation. Paleoceanography 7, 405–422.

Parnell-Turner, R., White, N., Henstock, T., Murton, B., Maclennan, J., Jones, S.M., 2014. A continuous 55-million-year record of transient mantle plume activity beneath Iceland. Nat. Geosci. 7, 914–919.

Pfeiffer, M., Lohmann, G., 2016. Greenland ice sheet influence on last interglacial climate: global sensitivity studies performed with an atmosphere–ocean general circulation model. Clim. Past 12, 1313–1338.

Pickart, R.S., Torres, D.J., Clarke, R.A., 2002. Hydrography of the Labrador Sea during active convection. J. Phys. Oceanogr. 32, 428–457.

Poore, H., Samworth, R., White, N., Jones, S., McCave, I., 2006. Neogene overflow of Northern Component Water at the Greenland-Scotland Ridge. Geochem. Geophys. Geosyst. 7.

Rahmstorf, S., 1995. Bifurcations of the Atlantic thermohaline circulation in response to changes in the hydrological cycle. Nature 378, 145.

Rahmstorf, S., 2006. Thermohaline Ocean circulation. In: Elias, S.A. (Ed.), Encyclopedia of Quaternary Sciences. Elsevier, Amsterdam.

Roeckner, E., Brokopf, R., Esch, M., Giorgetta, M., Hagemann, S., Kornblueh, L., Manzini, E., Schlese, U., Schulzweida, U., 2006. Sensitivity of simulated climate to horizontal and vertical resolution in the ECHAM5 atmosphere model. J. Climate 19, 3771–3791.

Scheffer, M., Brovkin, V., Cox, P.M., 2006. Positive feedback between global warming and atmospheric CO_2 concentration inferred from past climate change. Geophys. Res. Lett. 33, L10702.

Scher, H.D., Martin, E.E., 2004. Circulation in the Southern Ocean during the Paleogene inferred from neodymium isotopes. Earth Planet. Sci. Lett. 228, 391–405.

Scher, H.D., Martin, E.E., 2008. Oligocene deep water export from the North Atlantic and the development of the Antarctic Circumpolar Current examined with neodymium isotopes. Paleoceanography 23.

Schulz, M., Mudelsee, M., 2002. REDFIT: estimating red-noise spectra directly from unevenly spaced paleoclimatic time series. Comput. Geosci. 28, 421–426.

Scotese, C.R., Gahagan, L.M., Larson, R.L., 1988. Plate tectonic reconstructions of the Cretaceous and Cenozoic ocean basins. Tectonophysics 155, 27–48.

Sewall, J.v., Van De Wal, R., Van Der Zwan, K., Van Oosterhout, C., Dijkstra, H., Scotese, C., 2007. Climate model boundary conditions for four Cretaceous time slices. Clim. Past 3, 647–657.

Sexton, P.F., Wilson, P.A., Norris, R.D., 2006a. Testing the Cenozoic multisite composite δ^{18}O and δ^{13}C curves: new monospecific Eocene records from a single locality, Demerara Rise (Ocean Drilling program Leg 207). Paleoceanography 21.

Sexton, P.F., Wilson, P.A., Pearson, P.N., 2006b. Microstructural and geochemical perspectives on planktic foraminiferal preservation: "Glassy" versus "Frosty". Geochem. Geophys. Geosyst. 7.

Sigman, D.M., De Boer, A.M., Haug, G.H., 2007. Antarctic stratification, atmospheric water vapor, and Heinrich events: a hypothesis for late Pleistocene deglaciations. In: Ocean Circulation: Mechanisms and Impacts-Past and Future Changes of Meridional Overturning, pp. 335–349.

Sijp, W.P., England, M.H., Huber, M., 2011. Effect of the deepening of the Tasman Gateway on the global ocean. Paleoceanography 26.

Sloan, L.C., Huber, M., 2001. Eocene oceanic responses to orbital forcing on precessional time scales. Paleoceanography 16, 101–111.

Stampfli, G., Borel, G.D., Marchant, R., Mosar, J., 2002. Western Alps geological constraints on western Tethyan reconstructions. J. Virtual Explorer 8, 77.

Stein, R., Boucsein, B., Meyer, H., 2006. Anoxia and high primary production in the Paleogene central Arctic Ocean: first detailed records from Lomonosov Ridge. Geophys. Res. Lett. 33.

Stickley, C.E., St John, K., Koç, N., Jordan, R.W., Passchier, S., Pearce, R.B., Kearns, L.E., 2009. Evidence for middle Eocene Arctic sea ice from diatoms and ice-rafted debris. Nature 460, 376–379.

Thomas, D.J., 2004. Evidence for deep-water production in the North Pacific Ocean during the early Cenozoic warm interval. Nature 430, 65–68.

Thomas, D.J., Bralower, T.J., Jones, C.E., 2003. Neodymium isotopic reconstruction of late Paleocene–early Eocene thermohaline circulation. Earth Planet. Sci. Lett. 209, 309–322.

Toggweiler, J., Bjornsson, H., 2000. Drake Passage and palaeoclimate. J. Quat. Sci. 15, 319–328.

Toggweiler, J., Samuels, B., 1998. On the ocean's large-scale circulation near the limit of no vertical mixing. J. Phys. Oceanogr. 28, 1832–1852.

Tripati, A., Elderfield, H., 2005. Deep-sea temperature and circulation changes at the Paleocene–Eocene thermal maximum. Science 308, 1894–1898.

Tripati, A.K., Eagle, R.A., Morton, A., Dowdeswell, J.A., Atkinson, K.L., Bahé, Y., Dawber, C.F., Khadun, E., Shaw, R.M., Shorttle, O., 2008. Evidence for glaciation in the Northern Hemisphere back to 44 Ma from ice-rafted debris in the Greenland Sea. Earth Planet. Sci. Lett. 265, 112–122.

Tucholke, B., Vogt, P., 1979. Western North Atlantic: sedimentary evolution and aspects of tectonic history. Initial Rep. Deep Sea Drill. Proj. 43, 791–825.

Via, R.K., Thomas, D.J., 2006. Evolution of Atlantic thermohaline circulation: early Oligocene onset of deep-water production in the North Atlantic. Geology 34, 441–444.

Werner, M., Haese, B., Xu, X., Zhang, X., Butzin, M., Lohmann, G., 2016. Glacial–interglacial changes in H218O, HDO and deuterium excess–results from the fully coupled ECHAM5/MPI-OM Earth system model. Geosci. Model Dev. 9, 647–670.

Zachos, J., Pagani, M., Sloan, L., Thomas, E., Billups, K., 2001. Trends, rhythms, and aberrations in global climate 65 Ma to present. Science 292, 686–693.

Zhang, X., Lohmann, G., Knorr, G., Purcell, C., 2014. Abrupt glacial climate shifts controlled by ice sheet changes. Nature 512, 290–294.

Zickfeld, K., Eby, M., Weaver, A.J., 2008. Carbon-cycle feedbacks of changes in the Atlantic meridional overturning circulation under future atmospheric CO_2. Glob. Biogeochem. Cycles 22.